INTERNATIONAL JOURNAL FOR NUMERICAL METHODS IN FLUIDS
Int. J. Numer. Meth. Fluids 2009; **60**:539–564
Published online 17 September 2008 in Wiley InterScience (www.interscience.wiley.com). DOI: 10.1002/fld.1906

Experimental and numerical characterization of the flowfield in the large-scale UW live fire research facility

C. B. Devaud*,†, J. Weisinger, D. A. Johnson and E. J. Weckman

Department of Mechanical and Mechatronics Engineering, University of Waterloo, 200 University Avenue West, Waterloo, Ont., Canada N2L 3G1

SUMMARY

Recently, a large-scale (19.5 m × 15.4 m × 12.8 m) live fire research facility (LFRF) has been built at the University of Waterloo with the capabilities of conducting controlled and systematic experimental studies to investigate the behaviour of large fuel spill fires in crosswinds. The present work is focused on characterizing the wind generated by banked fans and the flowfield in the LFRF using experimental techniques and large eddy simulation (LES). Two configurations are examined: the empty enclosure and the enclosure with a large blocking object (cylinder) aligned perpendicular to the flow direction.

Detailed velocity measurements are provided throughout the facility. The experimental results show that the flowfield inside the empty enclosure is consistent with the behaviour of a bluff wall jet.

Three-dimensional LES are performed for the same two configurations. The experimental velocity profiles are used to set the inflow conditions in the calculations. The numerical predictions are all within the experimental uncertainty in the core region for the empty enclosure. For the case with the cylinder, the size of the wake is very well reproduced by the simulations and the shedding frequency corresponds to the value given in published experimental studies of a flow over free standing cylinders. The present LES model is also capable of predicting more detailed flow characteristics such as the stagnation and recirculation region, compared with what was achievable in the large-scale experiments. In the wake the time-averaged velocities from the LES results are overpredicted. Possible sources of discrepancy are discussed. Copyright © 2008 John Wiley & Sons, Ltd.

Received 8 May 2008; Revised 15 July 2008; Accepted 17 July 2008

KEY WORDS: large-scale facility; velocity measurements; crossflow; LES; flowfield

*Correspondence to: C. B. Devaud, Department of Mechanical and Mechatronics Engineering, University of Waterloo, 200 University Avenue West, Waterloo, Ont., Canada N2L 3G1.
†E-mail: cdevaud@uwaterloo.ca

Contract/grant sponsor: NSERC

1. INTRODUCTION

The present study is focused on characterizing the wind conditions and the flowfield in a large-scale test facility using experimental and numerical tools. This analysis forms a key component of current investigations into fire hazards related to transportation accidents. Wind conditions are known to affect the geometry and tilt of large fuel spill fires, and to influence the behaviour of the plume of smoke and hot gases. Controlled and systematic experiments are needed to determine how wind influences properties of the fire such as the mass burning rate of fuel and the heat release rate of the fire. To date, most experimental studies into the behaviour of large fuel spill fires have been performed outdoors. However, due to the difficulties associated with the accurate control of the external conditions, in particular the wind, and with the demanding amount of instrumentation required for such large-scale experiments, detailed experimental measurements of the flowfield are either incomplete or unavailable. Recently, a large-scale facility has been built at the University of Waterloo to address these issues. The large-scale live fire research facility (LFRF) is equipped with a system for generating controlled crosswinds and controlling ventilation conditions. This system includes six fans, each 1.98 m in diameter, banked three across by two high. They are independently controlled with variable speed drives and together they can supply up to $472\,m^3/s$ through the $19.5\,m \times 15.4\,m \times 12.8\,m$ high test enclosure.

Banked fan systems have been used to develop large area wind profiles with success in the past. These facilities fall into two classifications: those using a large number of fans in an attempt to simulate atmospheric boundary layer flow via feedback control of the fans [1–3] and those using a smaller number of fans to generate a flow through a large facility at a reduced cost as compared with using one very large custom-designed fan [4, 5]. Although the LFRF test enclosure is not a wind tunnel and was neither designed nor intended to meet the strict flow quality requirements usually imposed upon wind tunnels, it is functionally similar to a wind tunnel in many ways. Its purpose is to generate a controlled, repeatable flow field with known or measurable velocity distribution in which the interaction of the wind and large test objects can be studied. Therefore, the flow field must be carefully characterized before testing proceeds. For this purpose, the methods and requirements for the calibration of wind tunnel test sections provide a great deal of insight into the present requirements. Typically the static pressure, velocity or dynamic pressure, and the turbulence intensity need to be determined over the volume of the test section where the test object will be placed.

The first objective of this paper is to characterize the flowfield that is produced by the wind generation system in the LFRF. Detailed velocity measurements throughout the enclosure will be presented for two configurations: an empty facility and one with a large cylinder aligned perpendicular to the flow direction. The inclusion of the cylinder is to mimic a crossflow over a plane fuselage. All the measurements are made in isothermal conditions.

The second objective is to assess the capabilities of three-dimensional large eddy simulation (LES) to predict the complex flowfield in this large-scale enclosure. Detailed comparison of the computational results with the experimental data will be shown. It is crucial to develop and validate computational tools in close conjunction with experimental techniques in order to have a full set of tools available to study fluid flow and heat transfer in large-scale situations. A simulation run using a well-validated computational fluid dynamics (CFD) code can provide accurate information at any time and any point in space. Equivalent information may be difficult to retrieve from an experimental investigation. Within this framework, however, even our computational capabilities are limited since direct numerical simulations are still out of reach due to the wide range of length

DOI: 10.1002/fld

and time scales, which need to be fully resolved. Instead, CFD techniques based on Reynolds-averaged Navier–Stokes equations (RANS) and LES have been more commonly applied to flows with various degrees of complexity. RANS calculations are based on ensemble-averaged flow equations where the unclosed Reynolds stress tensor may be approximated using a two-equation eddy viscosity model such as k–ε, or a Reynolds stress formulation. In LES, the large turbulent flow structures containing most of the energy are resolved explicitly, while the dissipation scales are modelled. Consequently, the instantaneous resolved flowfield can be provided with great accuracy, whereas most of this information is lost in RANS. The experimental LFRF configuration is unique and no previous simulation for such large-scale enclosures has been reported. Many numerical studies, using RANS and LES for prediction of flow over different types of bluff-body, such as a square cylinder [6, 7], a matrix of cubes [8] and a triangular prism [9], obtained good predictions using LES and pointed out the weaknesses of RANS calculations, even with the inclusion of wall effects, around the stagnation and in the wake regions. For example, the size of the recirculation zone and the level of turbulent kinetic energy were not properly captured by Bosh and Rodi [7] and Cheng *et al.* [8]. Many LES studies focused on flow over a cylinder with a low Reynolds number, Re_D, based on the cylinder diameter where the boundary layer is laminar prior to separation. A good summary of these past results can be found in the work of Franke and Frank [10]. Very few investigations considered high Reynolds number flows where the boundary layer over the cylinder is much thinner compared with low Re cases. Breuer [11] applied LES to a flow over a cylinder at $Re_D = 1.4 \times 10^5$ using different subgrid models and several O-type orthogonal grids (between 1.7424×10^6 and 6.760×10^6 nodes). The boundary layer was still laminar and was fully resolved in the simulations without any wall model. Good agreement for the time-averaged velocity components was obtained with available experimental data in the near wake region. Catalano *et al.* [12] used LES for a range of Reynolds numbers (0.5, 1 and 2×10^6) including a wall model to approximate the boundary layer. They presented good results for the pressure and skin friction coefficients compared with experimental data but further numerical validation was limited due to the lack of experimental information related to the velocity field in the wake. They also noted some inconsistencies for the highest Reynolds number flow possibly due to the combined effect of grid resolution and the wall layer model. All these previous studies demonstrate that the flow past a circular cylinder is one of the most challenging and complex flowfields, although the geometry is simple. The flowfield includes large three-dimensional, geometry-vortex flow in the wake region, boundary-layer separation and recirculation. In the present study, additional effects resulting from the enclosure walls being close to the cylinder, the finite length of the cylinder and the proximity of the exit door to the wake region are expected to have an impact on the flowfield. These factors will be considered and discussed. The Reynolds number for the flow over the cylinder in the experimental facility is very high: 2.5×10^6.

2. EXPERIMENTAL FACILITY AND MEASUREMENT TECHNIQUES

2.1. Test enclosure

As shown in Figure 1, the large-scale test enclosure is 19.5 m long by 15.4 m wide. The wind generation system consists of a fan array and a plenum region (not shown in Figure 1, located upstream of the test area). The fan array is composed of six Howden-Buffalo Model 78-26 Series 1000 vane axial fans, each 1.98 m in diameter. They are arranged three across by two high. Each

DOI: 10.1002/fld

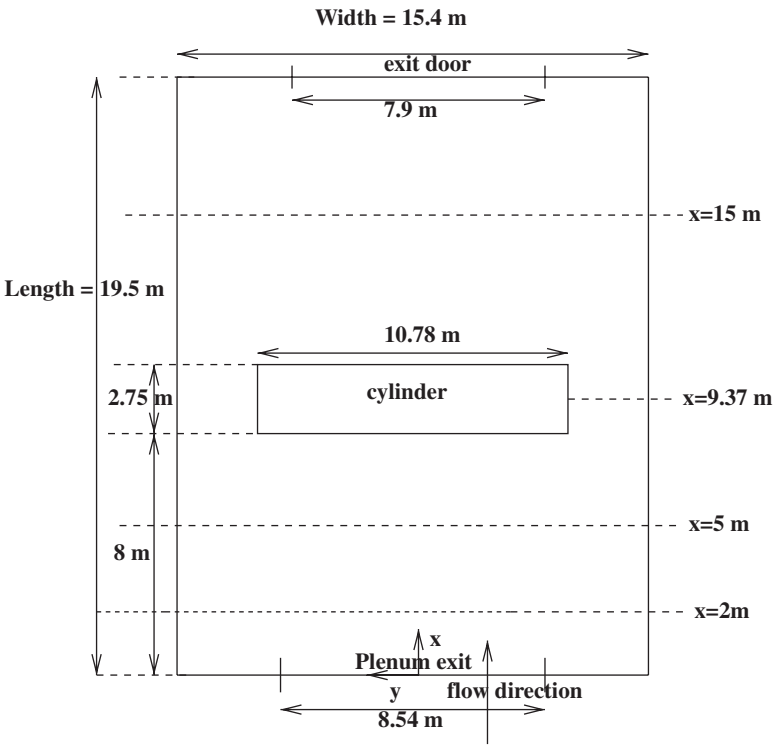

Figure 1. Schematic of the facility with the cylinder.

fan is rated to generate 78.7 m^3/s at 413.5 Pa, with an efficiency of 72%, a rotational speed of 1185 rpm, and brake horsepower of 100 hp. The fans charge an 8.23 m long by 8.54 m wide by 5.9 m high plenum. Flow conditioning in the plenum is provided by two settling screens and a seven across by five high array of steel flow-straightening ducts. The settling screens are located 3.6 m downwind of the fans and are separated by approximately 0.2 m. They are composed of 3.18 mm diameter galvanized steel wires forming 29 mm open squares, yielding 78% porosity. Two diagonal support members are located between the screens forming an 'X' structure reaching to the edges of the plenum. The flow-straightening ducts are located at the exit of the plenum, with dimensions approximately 1.18 m × 1.18 m and 1.83 m deep in the direction of the flow. The crosswind that is generated by the fan system exits the large-scale test area through a 7.9 m × 7.9 m overhead sectional door, indicated in Figure 1 as exit door. This door is open to atmospheric air at all times. The ceiling mimics a gable roof with a height of 7.8 m at the side walls and 12.8 m at the centre of the room; it is lined with corrugated steel.

2.2. Configuration of large blocking object

A number of wind characterization tests were conducted with a large, cylindrical blocking object located inside the test enclosure (see Figure 1). The cylinder is made of corrugated steel with a nominal diameter of 2.75 m. The cylinder is oriented such that its longitudinal axis is aligned with

DOI: 10.1002/fld

the y-direction. It is situated 9.37 m downwind of the plenum exit plane and raised 2.56 m above the ground. The cylinder is supported at this height by four stands. Each support stand is 0.91 m wide in the y-direction and 1.42 m deep in the x-direction. The centrelines of the four stands are located at the y-positions of -4.10, -1.64, 1.70, and 4.23 m.

2.3. Velocity measurement

Velocity measurements are made using bidirectional, low velocity probes used previously in fire and particle laden experiments [13]. The main limitation of the bidirectional probes is the low sampling frequency (2 Hz in the present study). However, this has to be counter-balanced with their robustness at high wind speeds and ability to sustain high temperatures for fire experiments. The dynamic pressure, temperature, and static pressure data are required for the calculation of velocity. Several probes were used because of the large area over which measurements are required in a given plane and the restrictions on available time. A single horizontal row of 16 probes is traversed vertically from top to bottom across each measurement plane. Each of the 16 bidirectional probes is connected to two Setra 267 pressure transducers mounted at the same height and therefore traversed with the probe itself. Pressure measurements are recorded using National Instruments Fieldpoint data acquisition modules. This technique represents the best possible compromise between the required test time, minimal flow blockage, and cost of instrumentation.

A value for the density of the air is required to reduce the measured dynamic pressure to velocity. Thus, the temperature of the air reaching the probes is also determined. Although it is not expected to vary significantly across the length of the beam in cold-flow characterization tests, one type-K thermocouple is placed near the sensing opening of each bidirectional probe. The thermocouple output is also recorded using the data acquisition modules mounted on either end of the probe beam.

Measurements are taken at four downstream positions for a total of 60 test runs and 960 measurement positions. The $x=2$ m plane is the closest plane to the plenum outlet ($x=0$) at which measurements could be made. The $x=5$, 10 and 15 m planes are chosen as intermediate x locations. In each of the aforementioned planes, measurements are made at heights between 0.6 and 6.0 m. Static taps of Pitot-static tubes are selected for the static pressure measurements. Six Pitot probes are attached to the instrumentation rig. To reduce errors due to misalignment [14], all six Pitot tubes are aligned within 5% of the x-direction prior to testing. The pressure sensed by the probes is measured using the Setra 267 pressure transducers.

The raw dynamic pressure and static pressure data are both recorded in the form of voltage outputs ranging from 0 to 10V. The dynamic pressure data are in the form of two data sets—one from the pressure transducer with a full-scale range of ± 250 Pa and the other from the pressure transducer with a full-scale range of ± 25 Pa. The ensemble average and standard deviation of each data set are calculated.

Measurements in the empty test enclosure are made at all four downwind measurement planes. Each time the six fans are turned on and run for at least 1 min to reach steady-state conditions before the start of the measurements. Data are collected at a rate of 2 Hz for a total time of 5 min at each downwind location. With the cylindrical blocking object in place, measurements are made at the $x=2, 5,$ and 15 m downstream locations.

2.4. Experimental uncertainty

Table I provides typical values for the bias error, precision error, and total uncertainty in average velocity in the central portion and near the edges of the flow field. The bias uncertainty in velocity

DOI: 10.1002/fld

Table I. Summary of the overall uncertainty in ensemble average velocity due to bias and precision errors and due to the test length.

	Bias error	Precision error	Total uncertainty	Error due to test length	Overall uncertainty
Central region	±3.0 to ±3.2%	±0.55 to ±0.70%	±3.1 to ±3.3%	±2.75%	±4.3%
Edge region	±15 to ±45%	±2.5 to ±10%	±15 to ±45%	±6.0%	±15 to ±45%

depends on the measured variables and their uncertainties and is calculated for each measurement point in time and space. Within each 5-min data set, the average of the bias uncertainty values is calculated and taken as the estimate of bias uncertainty of the ensemble average velocity at that location. Typically, the bias uncertainty is found to be between ±3.0 and ±3.2% of the ensemble average velocity.

The precision uncertainty is calculated based on estimates of three factors: the non-repeatability and thermal effects attributed to the pressure transducer, the quantization and noise introduced by the data acquisition system, and variation in the data set. The precision uncertainty falls between ±0.55 and ±0.70% of the average value in the central portion of the flow field. Near the edges of the flow field, the level of variation is observed to be greater than in the centre region. Values between ±2.5 and ±10% of the average velocity are determined.

A long test of approximately 20 min (1230 s) was conducted, during which dynamic pressure and temperature were measured to determine the effect on the ensemble averages. The test time had to be as short as possible due to the large number of tests required and the overall time constraints. However, if the test time was too short, then an insufficient number of samples would be available from each measurement location for the calculation of the ensemble average velocity and standard deviation of velocity. These parameters would then potentially deviate significantly from their theoretical values, which would be ideally calculated assuming an infinite number of data points. Owing to constraints on the total time available for velocity measurement experiments, each test was restricted in length to 5 min (300 s). The added uncertainty in the calculated value for ensemble average velocity due to the reduced test time was approximated. Near the edges of the measurement region, the percentage differences in the averages were between 3.5 and 6.0%. However, the maximum difference for the remainder of the data sets was only 2.7%, with typical values close to 1%. Based on this value, the increased uncertainty due to the choice of test length was conservatively estimated at ±6.0% of the reported averages at the edges of the flow field and ±2.75% of the reported averages in the core of the flow field. To summarize, the uncertainty of the ensemble average velocity values is about ±4.3% for the majority of measurement locations.

3. COMPUTATIONAL DETAILS

The LES code used in this study is the fire dynamics simulator (FDS) made available through National Institute of Standards and Technology (NIST). FDS solves the low-Mach number form of the compressible Navier–Stokes equations. The full details of the numerical code is described in [15], and here only its main features are briefly described. FDS has been previously used with success for a variety of reacting and non-reacting flows [16, 17]. The filtering process in

DOI: 10.1002/fld

LES introduces unclosed quantities that are not resolved, such as the subgrid Reynolds stress, the subgrid heat and mass flux, the combustion heat release rate and the radiation loss. In the present study, the flow under consideration is isothermal. Thus the approximations related to combustion and heat transfer are not discussed. The subgrid Reynolds stress, τ_{ij}, is modelled using a standard Smagorinsky model [18] where the subgrid scale eddy viscosity is calculated by

$$\mu_{\text{sgs}} = \rho C_{\text{s}}^2 \Delta^2 |S| \tag{1}$$

ρ is the density, C_{s} the Smagorinsky constant, $|S|$ the filtered the rate of strain and Δ the filter width defined as $(\Delta_x \ \Delta_y \ \Delta_z)^{1/3}$, where Δ_x, Δ_y, Δ_z correspond to the grid spacing in x-, y-, and z-directions, respectively. In the present calculations, C_{s} is set to 0.2.

The governing equations are advanced in time using a second-order Runge–Kutta, predictor–corrector algorithm. Spatial derivatives are estimated with second-order-accurate finite differences on a rectangular grid, with scalar quantities assigned to the centre of grid cells and velocity quantities assigned to cell faces. Convective terms are upwind-biased, based on a CFL condition, in the predictor step and downwind-biased in the corrector step. Diffusive terms are central-differenced. The Poisson equation is solved using a direct fast-Fourier-transform-based solver.

As shown in Figure 2, the computational domain size has dimensions of $18\,\text{m} \times 15\,\text{m} \times 12.8\,\text{m}$ and closely reproduces the experimental configuration. The origin of the x-axis is set to the exit of the plenum. The numerical structured grid representing the empty enclosure consists of a total of 3.450×10^6 nodes, with $180 \times 150 \times 128$ nodes in the x-, y- and z-directions, respectively, resulting in a filter width of 0.1 m. Further significant grid refinement is applied when the cylinder is included in the domain in order to capture the flow dynamics of the wake behind the obstacle. The smallest grid spacing applied is 0.05 m in every direction, producing a filter width of 0.05 m. The finest computational grid results in 12.696×10^6 nodes. Every grid is also kept uniform in all

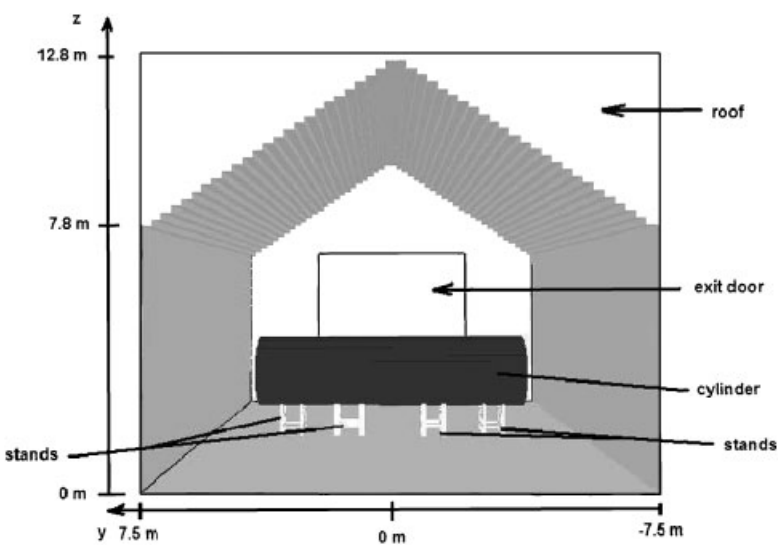

Figure 2. Computational domain including the cylinder and supports.

DOI: 10.1002/fld

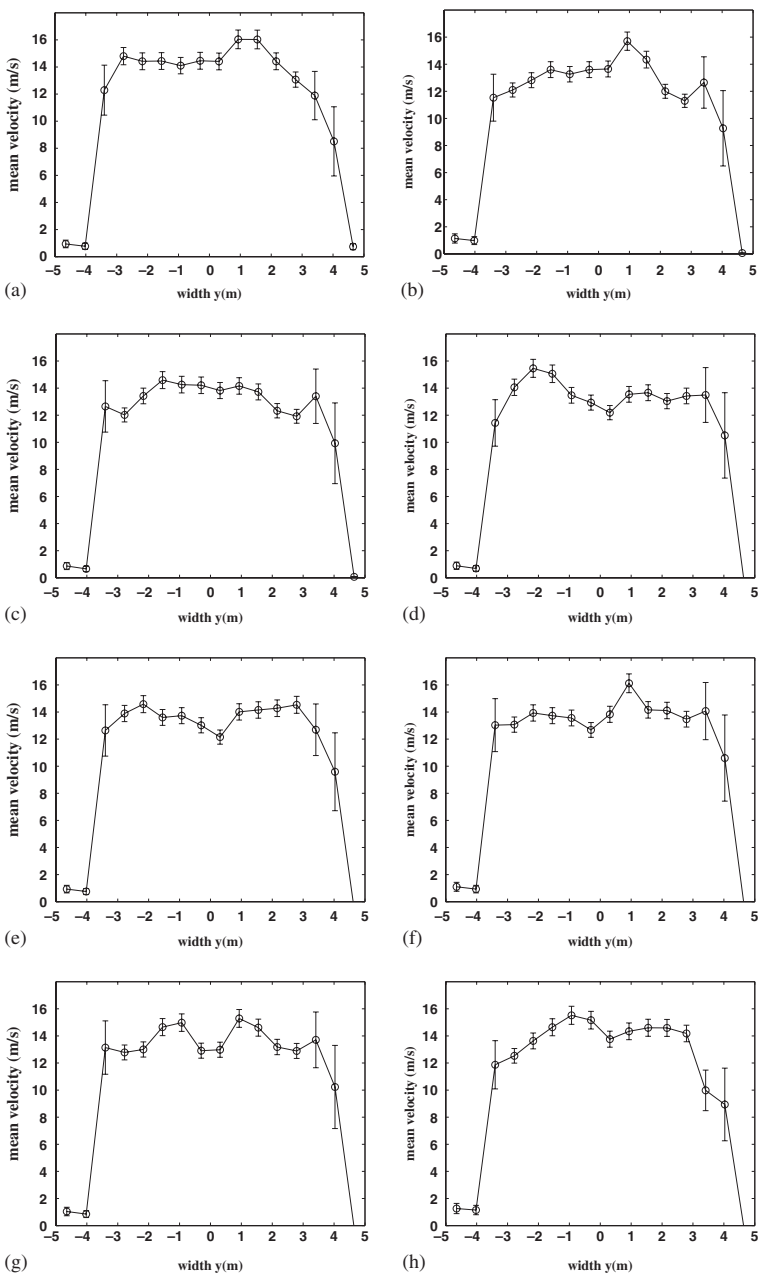

Figure 3. Empty enclosure-time-averaged velocity profiles at $x = 2\,\mathrm{m}$. Experimental data only used as boundary condition for LES: (a) $z = 0.6\,\mathrm{m}$; (b) $z = 1.2\,\mathrm{m}$; (c) $z = 1.8\,\mathrm{m}$; (d) $z = 2.4\,\mathrm{m}$; (e) $z = 3.0\,\mathrm{m}$; (f) $z = 3.6\,\mathrm{m}$; (g) $z = 4.2\,\mathrm{m}$; and (h) $z = 5.4\,\mathrm{m}$.

DOI: 10.1002/fld

directions to avoid any problem of permutation for the Fourier transforms in the code. The boundary layer on the wall and cylinder surfaces are not resolved but a partial slip boundary condition is applied in order to reproduce the wall effects. In the present LES implementation, the grid size determines the filter size, which separates the resolved large scales from the modelled small scales. It should lie in the inertial range of scales, beyond the energetic but larger than the dissipation scales. Grid sensitivity tests were performed and the results will be shown in Section 5.2. The inlet velocity conditions are set to match the velocity profiles measured very close to the plenum exit, i.e. at $x=2$ m, shown in Figures 3 and 8 for the empty enclosure and the enclosure with the cylinder, respectively. The exit door is defined as a free open boundary. The initial condition is still air at 20°C and 1 atm. Turbulence is generated at the start of the calculations in FDS. Random vorticity fluctuations are added to the flowfield in the entire computational domain. A sensitivity analysis was performed in order to measure the impact of the fluctuation level on the time-averaged velocities. Negligible differences were noticed. There is no time-dependent boundary condition in the present simulations. Depending on the CPU and RAM requirements of the simulations, single or multiple XEON processors are used and the run CPU times approximately vary between 100 and 300 h for 300 s of simulated flow. FDS uses adaptive time steps based on a CFL condition. Typical time steps are on the order of 0.004 s for the empty enclosure and 0.0014 s for the case with the cylinder. For comparison with the experimental data, the LES results are time-averaged over 290 s (the early data are removed) using a sampling frequency of 2 Hz, as is employed in the experiments.

4. VELOCITY FIELD IN THE EMPTY ENCLOSURE

4.1. Experimental results

Time-averaged experimental data are shown in Figures 3–6 for the four traversing planes: $x=2$, 5, 10 and 15 m, respectively. At the plane closest to the plenum exit ($x=2$ m), the experimental measurements show that the velocities are not perfectly uniform. Three distinct peaks can be seen in the profiles; at $y\simeq 1$ m with a magnitude of around 16 m/s for $z\leqslant 1.2$ m and $3.6\,\text{m}\leqslant z\leqslant 4.2$ m, at $y\simeq -2.2$ m with a velocity magnitude of around 15 m/s for $1.8\,\text{m}\leqslant z\leqslant 3.0$ m and at $y\simeq -1$ m of around 15 m/s for $4.2\,\text{m}\leqslant z\leqslant 5.4$ m. This observation leads to the conclusion that the jets issuing from the six fans further upstream have not entirely merged to a single jet configuration by the exit of the plenum area. The first three lower fans are aligned and centred at $z=1.5$ m and at $y=-2.9, 0, 2.86$ m. The upper fans are centred at $z=4.42$ m for the same y locations as for the lower elements. This layout results in two sets of three parallel jets. Depending on the relative strength of the centre to outer jets, parallel jets may act differently. Tanaka and Nakata [19] studied three parallel jets and showed that when the velocity of the centre jet was less than the velocity of the outer two jets, the centre jet attached to one of the outer jets and the remaining two jets behaved as an asymmetric dual jet flow. Thus, the velocity profiles in Figure 3 suggest that the centre fans run at a lower flowrate and the jets from the centre fan and that centred at $y=2.86$ m merge. Further, a small depression in the magnitude of the wind velocity can be seen near the centre of the plane (roughly encompassed by the region $-0.5\,\text{m}<y<0.7$ m for heights between 2.4 and 4.4 m). Although this region of low velocity may have resulted from complex interactions between the six fans of the wind generation system or may have been an indication of a bluff jet effect, its position seems to correlate very well with the centre of the 'X'-shaped support member

DOI: 10.1002/fld

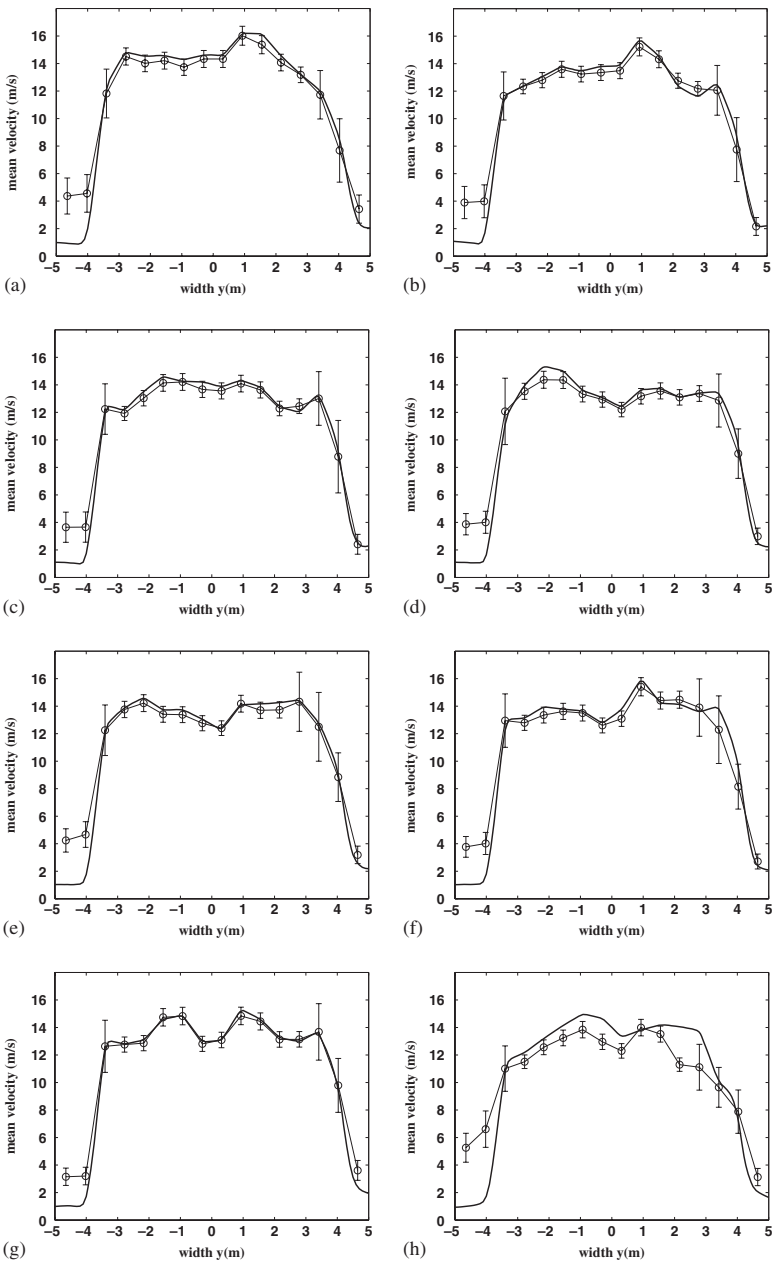

Figure 4. Empty enclosure-time-averaged velocity profiles at $x = 5\,\text{m}$, Exp: line with open symbols and LES: solid line. (a) $z = 0.6\,\text{m}$; (b) $z = 1.2\,\text{m}$; (c) $z = 1.8\,\text{m}$; (d) $z = 2.4\,\text{m}$; (e) $z = 3.0\,\text{m}$; (f) $z = 3.6\,\text{m}$; (g) $z = 4.2\,\text{m}$; and (h) $z = 5.4\,\text{m}$.

DOI: 10.1002/fld

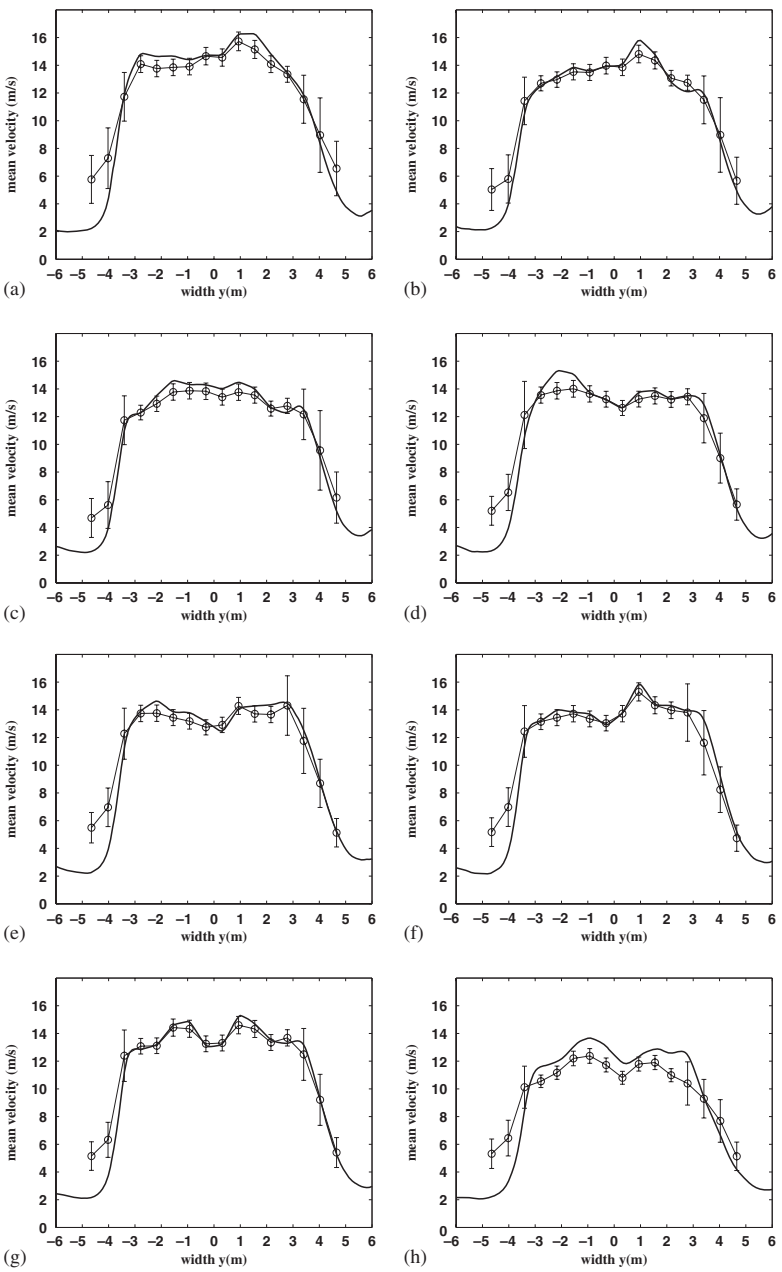

Figure 5. Empty enclosure-time-averaged velocity profiles at $x = 10\,\text{m}$, Exp: line with open symbols and LES: solid line. (a) $z = 0.6\,\text{m}$; (b) $z = 1.2\,\text{m}$; (c) $z = 1.8\,\text{m}$; (d) $z = 2.4\,\text{m}$; (e) $z = 3.0\,\text{m}$; (f) $z = 3.6\,\text{m}$; (g) $z = 4.2\,\text{m}$; and (h) $z = 5.4\,\text{m}$.

DOI: 10.1002/fld

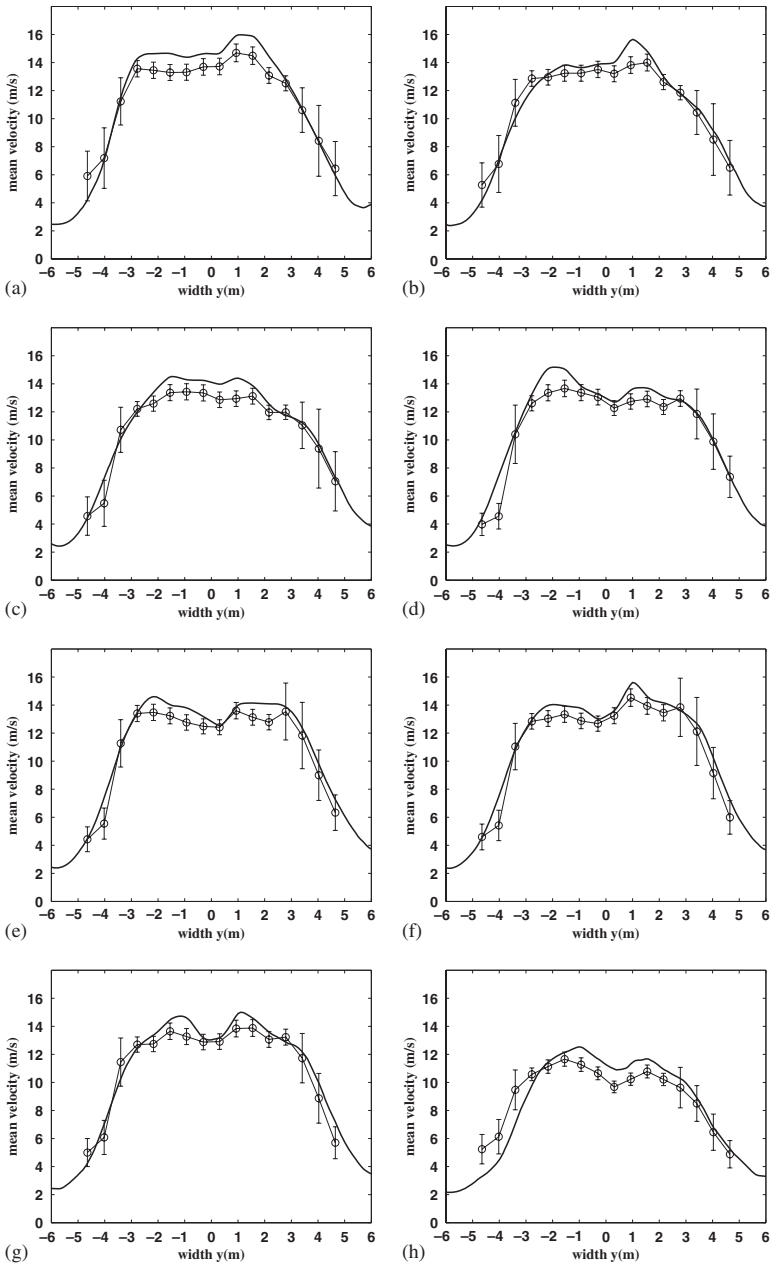

Figure 6. Empty enclosure-time-averaged velocity profiles at $x = 15\,\mathrm{m}$, Exp: line with open symbols and LES: solid line. (a) $z = 0.6\,\mathrm{m}$; (b) $z = 1.2\,\mathrm{m}$; (c) $z = 1.8\,\mathrm{m}$; (d) $z = 2.4\,\mathrm{m}$; (e) $z = 3.0\,\mathrm{m}$; (f) $z = 3.6\,\mathrm{m}$; (g) $z = 4.2\,\mathrm{m}$; and (h) $z = 5.4\,\mathrm{m}$.

DOI: 10.1002/fld

Table II. The spatially averaged mean velocity in the core area of the flow field.

	Extent of core region		Time-averaged velocity
x (m)	y-range (m)	z-range (m)	Experimental value (m/s)
2.00	$-3.4 \leqslant y \leqslant 3.4$	$z \leqslant 5.4$	13.7
5.00	$-3.4 \leqslant y \leqslant 3.4$	$z \leqslant 5.4$	13.4
10.00	$-3.4 \leqslant y \leqslant 3.4$	$z \leqslant 4.8$	13.4
15.00	$-2.8 \leqslant y \leqslant 2.8$	$z \leqslant 4.8$	13.1

in the plenum (at $y=0$ and $z=2.86\,\text{m}$). Therefore, this velocity deficit may actually delineate the wake of this cross support.

Aside from the fairly isolated regions of reduced and elevated velocities that arise due to the physical features of the facility, the profiles shown in Figures 3–6 generally show similar trends to those seen for a three-dimensional, bluff wall jet [20]. The core of the flow field diminishes in size with increasing distance downstream. Table II summarizes the extent of the core region at the different planes. At $x=2\,\text{m}$ the core region is bounded by $-3.4\,\text{m}<y<3.4\,\text{m}$ and $z \leqslant 5.4\,\text{m}$, whereas at the $x=15.0\,\text{m}$ plane the core region is bounded by $-2.8\,\text{m}<y<2.8\,\text{m}$ and $z \leqslant 4.8\,\text{m}$. Owing to entrainment and mixing, the velocity gradients at the edges of the flow field become less steep with distance downstream. Therefore, the overall flow field issuing from the plenum increases in size as x increases, which is also consistent with the expected behaviour of a bluff wall jet [20].

4.2. LES results

The time-averaged velocities obtained using FDS are compared with the experimental data in Figures 3–6. The inlet boundary conditions and the 3D-reproduction of the experimental enclosure used in the present calculations have a significant impact in the present simulations. The experimental time-averaged velocities measured at $x=2\,\text{m}$ are used as inlet conditions (at $x=0\,\text{m}$) in the calculations. The inlet velocities are not uniform and it would have been impossible to determine numerically the present inlet conditions without any experimental measurements. Further, the whole enclosure is modelled including the complex shape of the roof. Simplified geometries using a flat roof or a symmetry plane were tested and results were shown to be very sensitive to these changes. Hence, the entire enclosure is used for all simulations reported here.

In Figures 4–6 some differences between simulated and experimental time-averaged velocities can be seen at the edges of the jet. However, the predicted values remain within the experimental uncertainty. At $x=15\,\text{m}$, the time-averaged velocities from LES slightly overpredict experimental data in the core region, at most 14%, whereas the experimental uncertainty is estimated to be around 4%. This would mean that the simulated mixing rate with the surroundings is slightly lower than in the experiments.

Figure 7(a)–(d) present snapshots of the instantaneous velocity magnitude at the four planes of interest, i.e. $x=2$, 5, 10 and 15 m. As shown, very little mixing occurs between the core and exterior region at the first two planes. Further downstream, significant mixing and flow recirculation can be seen at the flow edges and in the roof area. At $x=15\,\text{m}$, the jet core is greatly distorted due to mixing with exterior fluid.

DOI: 10.1002/fld

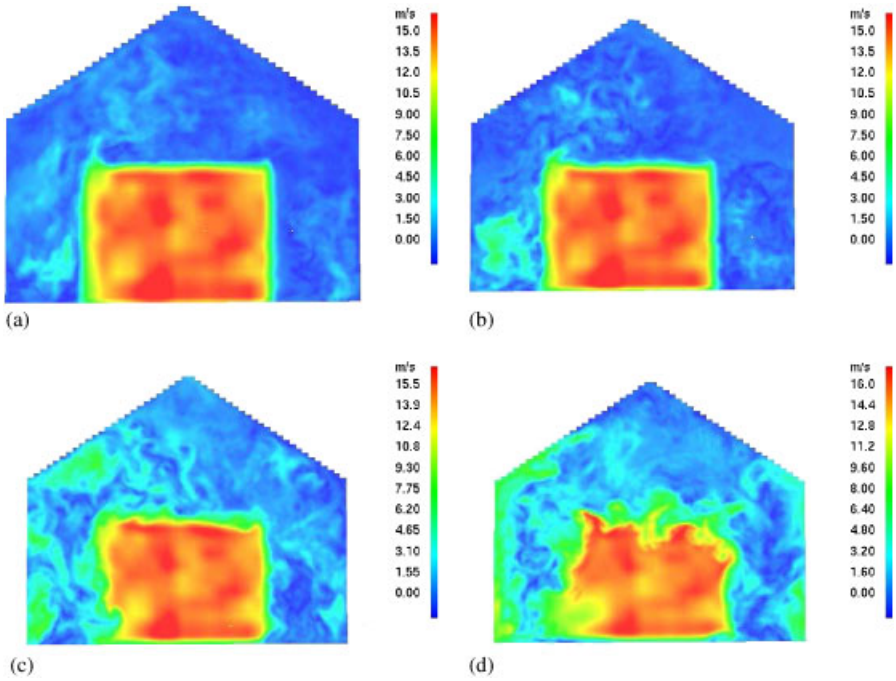

Figure 7. Empty enclosure-instantaneous velocity contours at time = 120 s at several planes across the facility: (a) $x = 2$ m; (b) $x = 5$ m; (c) $x = 10$ m; and (d) $x = 15$ m.

5. VELOCITY FIELD IN THE ENCLOSURE WITH THE LARGE OBJECT

5.1. Experimental results

Velocity measurements in the test enclosure with the cylindrical blocking object present are made across the y–z plane at each of three downwind locations: $x = 2, 5$ and 15 m. The ensemble-averaged velocity profiles are shown in Figures 8–10, respectively. In general, the velocity profiles upwind of the cylinder are similar to the velocity profiles at the same locations within the empty test enclosure shown in Figures 3 and 4. At $x = 2$ m (Figure 8) the velocity is not influenced significantly by the addition of the blocking object into the test enclosure. Compared to the values presented in Figure 3, the velocity decreases by less than 1 m/s within the majority of the measurement area. The averaged velocity in the core region is calculated to be 13.2 m/s instead of 13.7 m/s (see Table II) for the same plane ($x = 2$ m) in the empty enclosure. Nonetheless, the cylinder represents a large stagnation surface in the flow. As the flow approaches the surface, the pressure is expected to increase and the velocity to decrease. Thus, the small observed decrease in velocity is consistent with the anticipated trend. At $x = 5$ m (Figure 9) the velocity in the core region decreases moderately with the addition of the blocking object compared to that in Figure 6. In the centre of the flow field, i.e $y \simeq 0$ m and at heights near the centreline of the cylinder ($2.4\,\text{m} \leqslant z \leqslant 3.6\,\text{m}$), the velocity decrease can reach values between 2 and 3.4 m/s. The spatially averaged velocity over the core region at this plane is 12.20 m/s, whereas the value of 13.4 m/s was found for the flow in the empty enclosure (Table II). This observation also follows the expected trend of increasing

DOI: 10.1002/fld

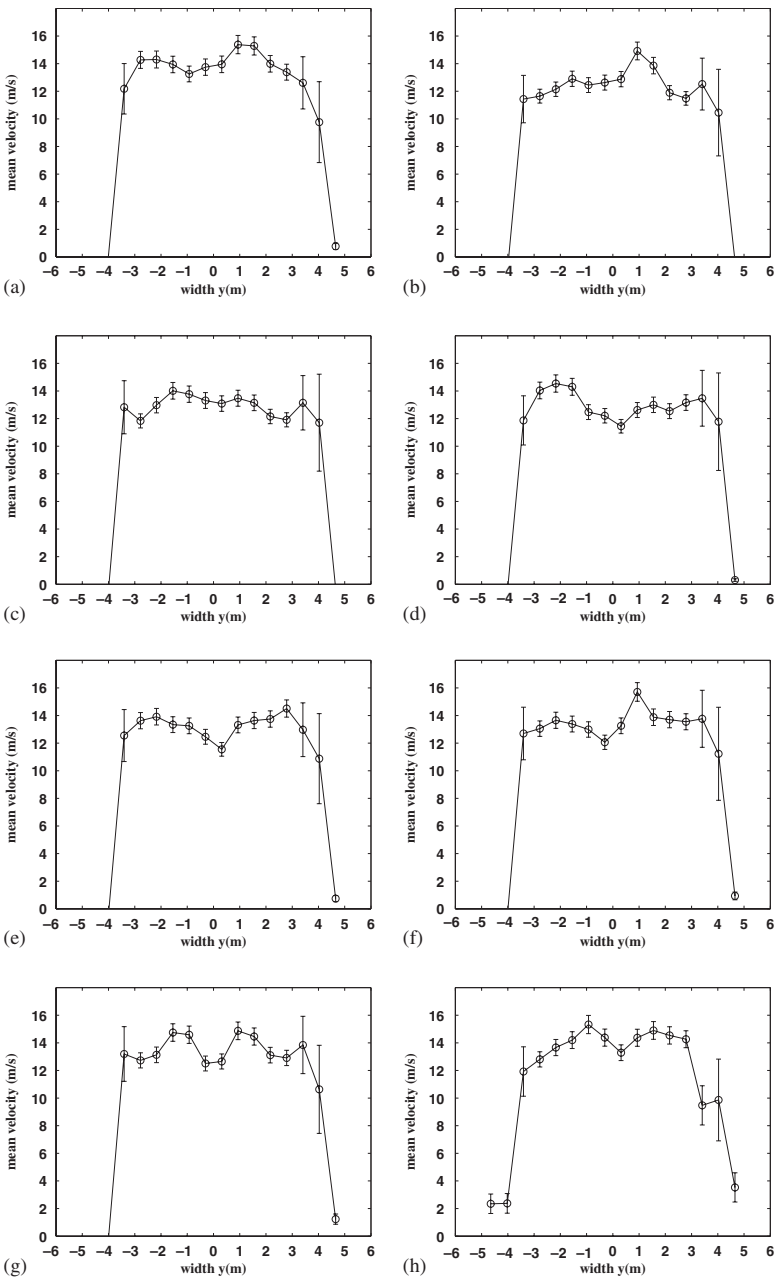

Figure 8. With cylinder-time-averaged velocity profiles at $x = 2$ m. Experimental data only, used as boundary condition for LES: (a) $z = 0.6$ m; (b) $z = 1.2$ m; (c) $z = 1.8$ m; (d) $z = 2.4$ m; (e) $z = 3.0$ m; (f) $z = 3.6$ m; (g) $z = 4.2$ m; and (h) $z = 5.4$ m.

DOI: 10.1002/fld

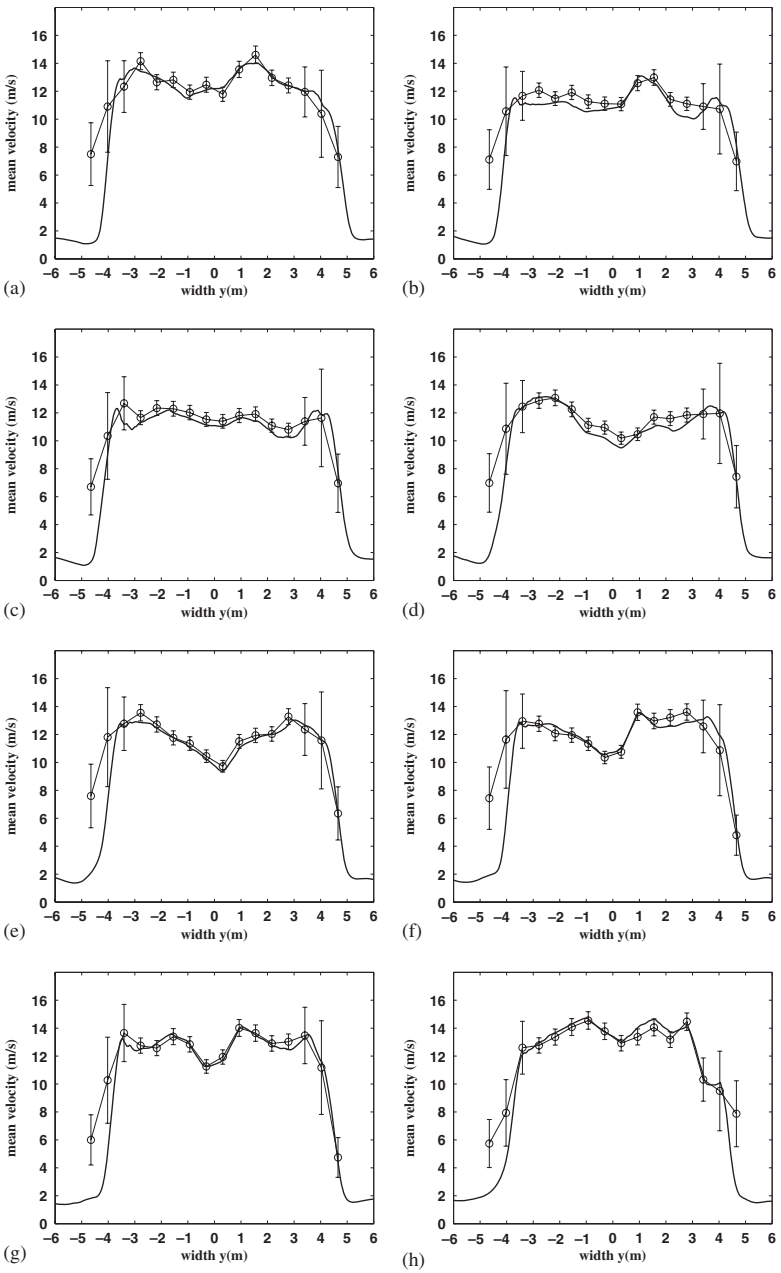

Figure 9. With cylinder-time-averaged velocity profiles at $x=5\,\mathrm{m}$, Exp: line with open symbols and LES: solid line. (a) $z=0.6\,\mathrm{m}$; (b) $z=1.2\,\mathrm{m}$; (c) $z=1.8\,\mathrm{m}$; (d) $z=2.4\,\mathrm{m}$; (e) $z=3.0\,\mathrm{m}$; (f) $z=3.6\,\mathrm{m}$; (g) $z=4.2\,\mathrm{m}$; and (h) $z=5.4\,\mathrm{m}$.

DOI: 10.1002/fld

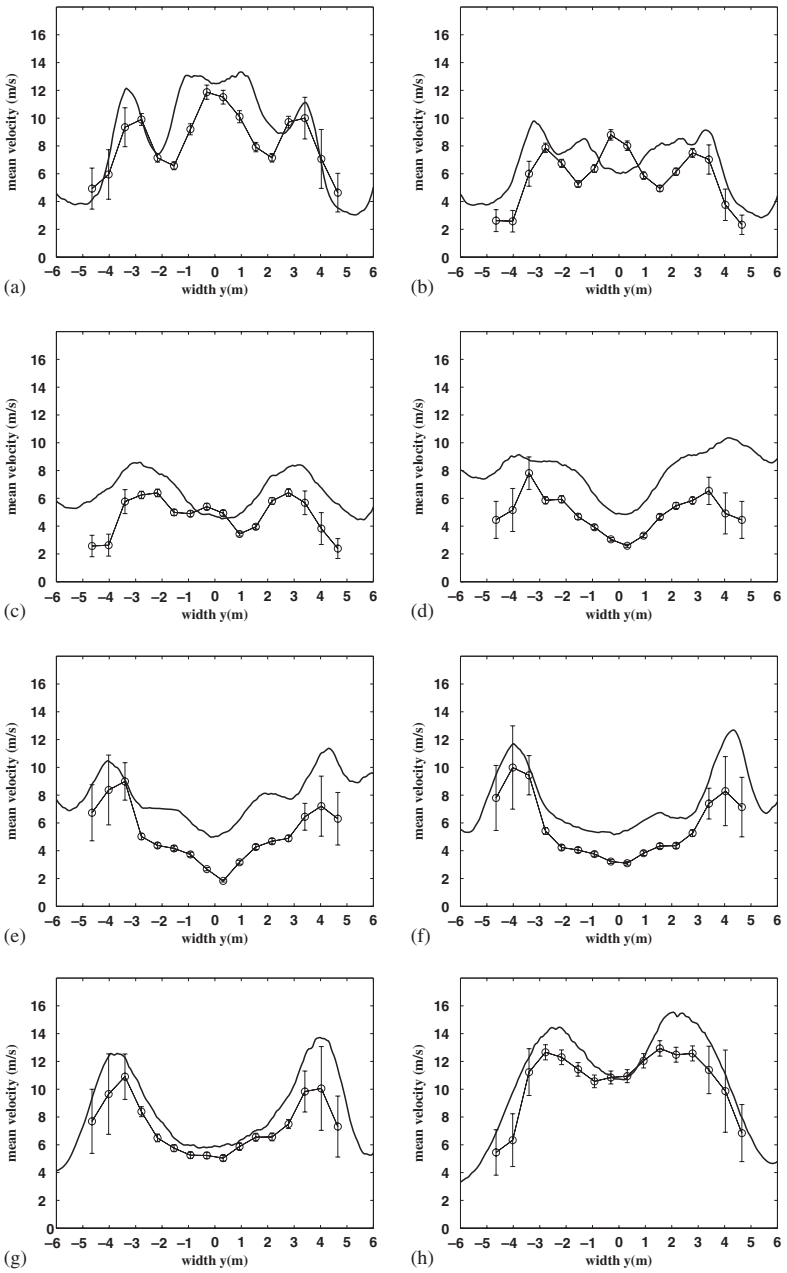

Figure 10. With cylinder-time-averaged velocity profiles at $x = 15\,\mathrm{m}$, Exp: line with open symbols and LES: solid line. (a) $z = 0.6\,\mathrm{m}$; (b) $z = 1.2\,\mathrm{m}$; (c) $z = 1.8\,\mathrm{m}$; (d) $z = 2.4\,\mathrm{m}$; (e) $z = 3.0\,\mathrm{m}$; (f) $z = 3.6\,\mathrm{m}$; (g) $z = 4.2\,\mathrm{m}$; and (h) $z = 5.4\,\mathrm{m}$.

DOI: 10.1002/fld

pressure and decreasing velocity approaching the surface of the cylinder. At $x=15\,\text{m}$, as shown in Figure 10, a large wake is present and is characterized by much lower velocities than those in the core region upstream of the cylinder. These low velocities (between 2 and 4 m/s) are found within the region $-3\,\text{m}\leqslant y\leqslant 3.0\,\text{m}$ and $1.2\,\text{m}<z<4.80\,\text{m}$. Compared to the profiles without any object at the same location (Figure 6), the velocity decreases by as much as 10.7 m/s (approximately 85% velocity decrease). The lower and upper edges of the cylinder are at $z=1.18\,\text{m}$ and $z=3.93\,\text{m}$, respectively, and these dimensions agree well with the size of the wake seen in the experimental data. Two additional smaller regions exhibiting low velocities are seen at lower heights ($z\leqslant 1.2\,\text{m}$) for $-2.75\,\text{m}<y<-1.25\,\text{m}$ and $1.00\,\text{m}<y<2.50\,\text{m}$. These areas correspond to the wakes produced by the stands on which the cylinder is supported upstream, which partially blocks the flow from $-2.0\,\text{m}<y<-1.17\,\text{m}$ and $1.25\,\text{m}<y<2.16\,\text{m}$. These wake regions merge with the wake of the large cylinder with increasing height above the facility door.

5.2. LES results

In Figures 8–10, the time-averaged velocities are compared with the available experimental data at $x=2$, 5 and 15 m, respectively. For the first two planes (Figures 8 and 9) the differences between the experimental and numerical values are small and remain within the experimental uncertainty in the core region ($-4\,\text{m}\leqslant y\leqslant 4\,\text{m}$) although differences are more marked at $x=5\,\text{m}$ (Figure 9). At $x=15\,\text{m}$ (Figure 10), the shape of the velocity profiles is very well reproduced everywhere except at $z=1.2\,\text{m}$. The large wake produced by the cylinder is clearly shown for heights above 1.2 m, with low velocities between 5 and 6 m/s. The velocity magnitude is overpredicted compared to the experimental values, in particular for heights below 3 m. However, the size of the wake is well captured by the simulations compared to the experimental profiles. Close to the floor, the two wakes due to the support stands are also shown at $z=0.6\,\text{m}$. There seems to be a small shift in the y-direction in the computational profiles compared to the experimental data. This may be due to the simplified geometry of the stands used in the simulations. At $z=1.2\,\text{m}$ these wakes are not present anymore. Best agreement between the LES and experimental results is achieved for the upper half of the wake region, i.e. for $3.6\,\text{m}\leqslant z\leqslant 5.4\,\text{m}$. Several parameters may explain the overprediction of the velocity in the present LES results. The boundary layer is not fully resolved; a partial velocity slip is imposed at the wall surfaces. It is difficult to know the exact impact of this approximation on the predicted velocities in the wake. In order to reproduce the boundary layer, a very fine grid would need to be used in the near-wall region. In the present case, given the size of the entire enclosure, it is beyond our computational capabilities to take this into account given that the number of grid points in the near-wall region varies with the square of the friction Reynolds number [21]. One alternative would be to include a wall-layer model as used by Catalano *et al.* [12]. Further investigation is needed to determine the most suitable model and implementation for the current flow. In order to test the grid sensitivity, two different grids were employed: 0.1 m (grid 1) and 0.05 m (grid 2, the current grid). At $x=2$ and 5 m, no differences can be distinguished between the two sets of time-averaged velocities. Figure 11 presents the time-averaged velocities in the wake region, at $x=15\,\text{m}$, for the two meshes. Both grids reproduce the general features of the wake and it is not obvious which grid really yields the best results compared with the experimental values. At $z=0.6\,\text{m}$ the profiles obtained from grid 2 are closer to the experimental values but at $z=3.6\,\text{m}$ the results from grid 1 are better. A similar observation was reported by Breuer [11] where grid refinement did not necessarily lead to better predictions. Another aspect to consider when the accuracy of the grid is to be evaluated is to examine the energy spectrum produced by

DOI: 10.1002/fld

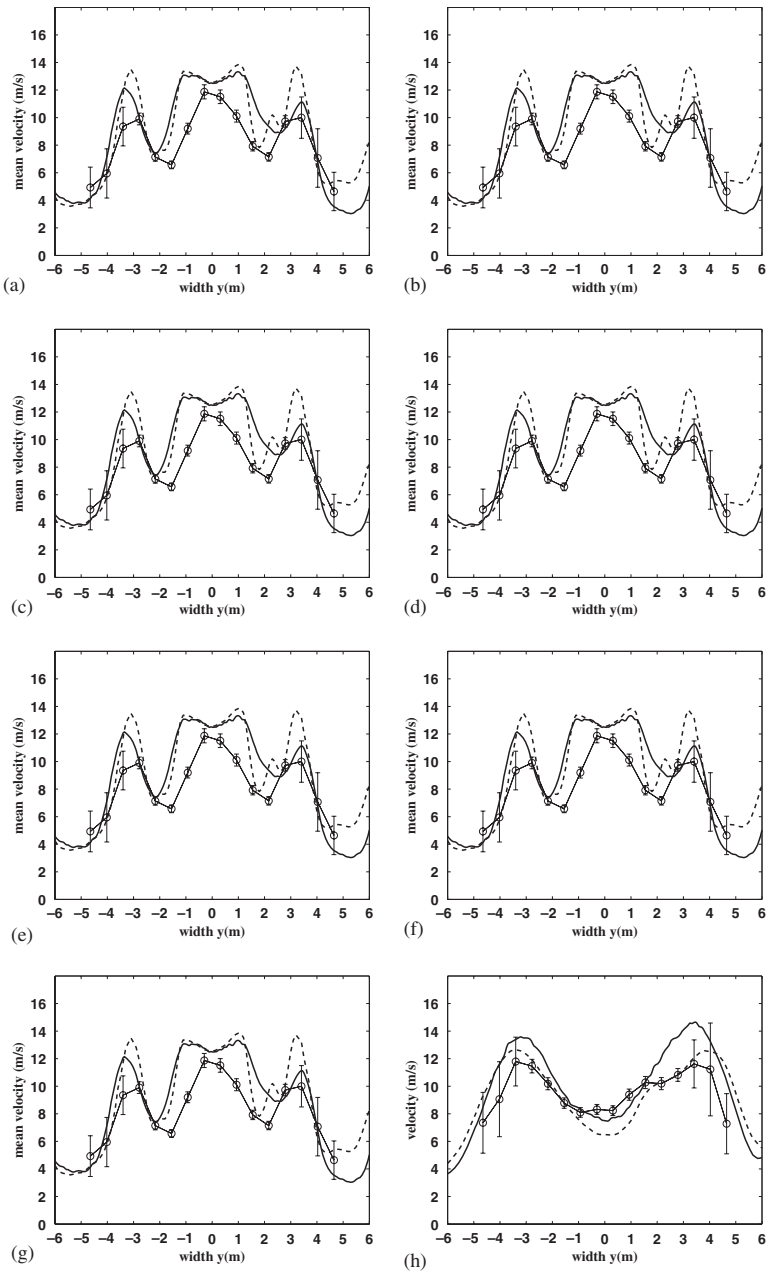

Figure 11. With cylinder-time-averaged velocity profiles at $x = 15$ m, Exp: line with open symbols, LES grid 2: solid line and LES grid 1: dashed line. (a) $z = 0.6$ m; (b) $z = 1.2$ m; (c) $z = 1.8$ m; (d) $z = 2.4$ m; (e) $z = 3.0$ m; (f) $z = 3.6$ m; (g) $z = 4.2$ m; and (h) $z = 5.4$ m.

DOI: 10.1002/fld

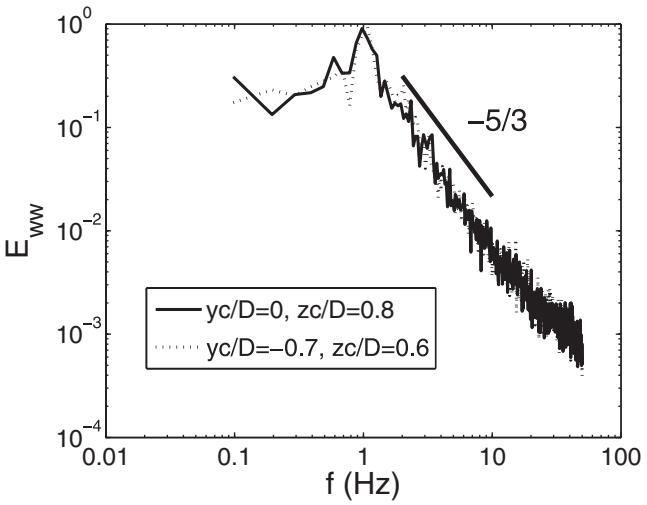

Figure 12. Frequency spectrum of the vertical velocity in the wake region at $x = 15\,\mathrm{m}$ ($\simeq 2D$) at two different positions. LES results only.

the simulations. LES is expected to fully resolve the large flow scales with a filter cutoff located somewhere in the inertial region of an energy spectrum. As can be seen in Figure 12, part of the inertial subrange is visible in the velocity frequency spectra, which indicates that the current grid is not too coarse. The Smagorinsky constant in the subgrid scale model is a well-known weakness since the value of the constant would need to be adjusted throughout the domain (dynamic model). However, there is no clear evidence in previous research that a dynamic subgrid scale model would lead to significantly improved predictions for the current flow situation [11, 22].

5.3. Shedding frequency

The Reynolds number for the flow under study, based on the diameter of the cylinder and an approximate wind velocity of 13.5 m/s, is $Re_D \approx 2.5 \times 10^6$. Regular and periodic vortex shedding has been observed from cylinders in crossflow. This phenomenon is known as a Karman vortex street. Experimental studies tend towards a Strouhal number around 0.2 for rough cylinders at high Reynolds number but for smooth cylinders vortex shedding was not observed for the supercritical regime [23, 24]. However, it should be noted that a wide range of Strouhal numbers between 0.18 and 0.50 can be found in the literature [25]. The large scatter in the experimental values is due to the fact that the flow around a cylinder depends on a variety of factors, such as the Reynolds number, the aspect ratio (length to diameter of the cylinder), the blockage ratio, the end conditions, the roughness of the cylinder, the free-stream turbulence level and the Mach number. In the present conditions the cylinder has an aspect ratio of 4 with the enclosure walls being at $0.7D$ away from the edges of the cylinder in the spanwise direction, $0.4D$ from the floor and $1.5D - 3D$ from the roof. Thus, the cylinder cannot be considered infinite and the enclosure walls are expected to affect the flow. Although some differences exist between previous experimental and present numerical conditions, useful indications for the evaluation of the simulations can be provided.

DOI: 10.1002/fld

Owing to the probe-transducer tubing lengths, the sampling frequency of 2 Hz in the experimental measurements is too low to perform a spectral analysis of the measurement turbulent velocity signals. As an alternative, smoke visualization is used during the experiments in order to identify possible vortex structures in the flow. Figure 13 shows one example of a vortex developing from the top of the cylinder and moving down to the wake region; however, no specific frequency of vortex formation could be observed in the experimental images. LES can provide data at much smaller time intervals. For that purpose the instantaneous velocity components are collected from the simulations at a frequency of 100 Hz. Figure 12 shows the frequency spectrum of the predicted vertical velocity at $xc/D=2$ ($x=15\,\mathrm{m}$) for two positions. For consistency with the standard notation used in previous studies of flow over a cylinder, the distances are normalized by the diameter of the cylinder and the origin of the coordinates is at the centre of the cylinder. For clarity, this new coordinate system is presented in Figure 14. As shown in Figure 12, a distinct peak is observed at a frequency of 1 Hz resulting in $St \simeq 0.2$, which agrees well with the value given by Roshko [23] and Shih *et al.* [24].

5.4. Flow structure using LES

Further information on the flow structure in the LFRF can be retrieved from the present LES results. Such information would be much more difficult to obtain from the experiments due to the scale of the present facility. Figure 15 shows the time-averaged streamwise velocity at the centre plane ($y=0\,\mathrm{m}$) of the facility. The spatial resolution (0.05–0.1 m) is much finer in the simulations than that achievable in the experimental measurements. The simulated flow reproduces qualitatively the expected flow behaviour. Upstream of the cylinder, the flow decelerates when approaching the object and the stagnation point can be identified. Since the boundary layer is not fully resolved, it is not possible to clearly identify the separation points. Figure 16 shows the time-averaged velocity vectors superimposed on the time-averaged streamwise velocity contours at $x=15\,\mathrm{m}$. A near-symmetric velocity field about $y=0$ can be seen. The in-plane velocity vectors show evidence of a single pair of counter rotating longitudinal vortices centred at ($y=2\,\mathrm{m}$, $z=4\,\mathrm{m}$) and ($y=-2\,\mathrm{m}$, $z=4\,\mathrm{m}$). Two smaller counter rotating longitudinal vortices are located beneath the cylinder at ($y=1.25\,\mathrm{m}$, $z=1.5\,\mathrm{m}$) and ($y=-0.5\,\mathrm{m}$, $z=1.5\,\mathrm{m}$). A larger 'curved' spanwise vortex is shown above the cylinder in this plane as evidenced by the magnitude of the streamwise velocity contours and the in-plane velocity components. It is not a complete spanwise vortex as defined by Huang *et al.* [26] as it is deformed from the cylinder end effects and the close wall boundaries.

6. CONCLUSIONS

A large test facility for the study of objects in crosswinds has been characterized. The experiments provided detailed flowfield information in the facility. This is the first step before investigating the effects of fire spread and heat release on an object in the flowfield for the same configurations. Further measurements are in progress in order to map the velocity field in the enclosure, for different wind velocities with and without the blocking object. Velocity fluctuations will also be collected at several locations using sonic anemometers. This will provide valuable information on the turbulence levels throughout in the flowfields.

For comparison, 3D LES with a standard Smagorinsky model was applied to the experimental configuration using similar test conditions. Agreement between the experimental data and the

DOI: 10.1002/fld

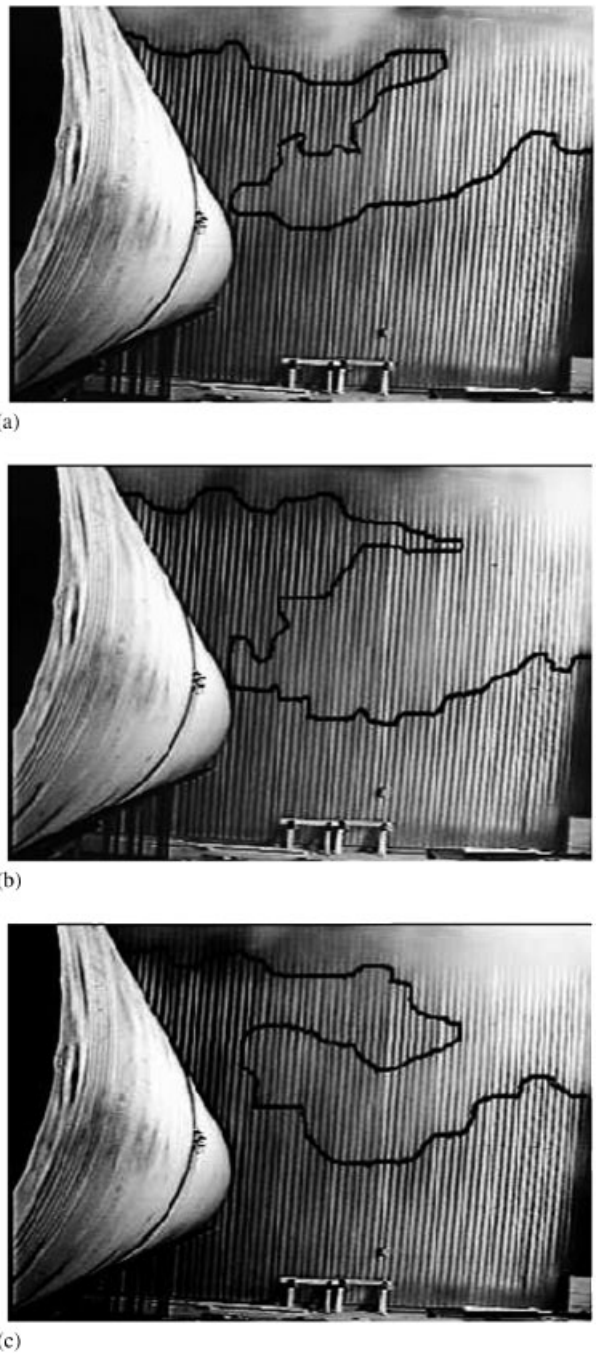

Figure 13. Smoke visualization downstream of the culvert at three different times.

DOI: 10.1002/fld

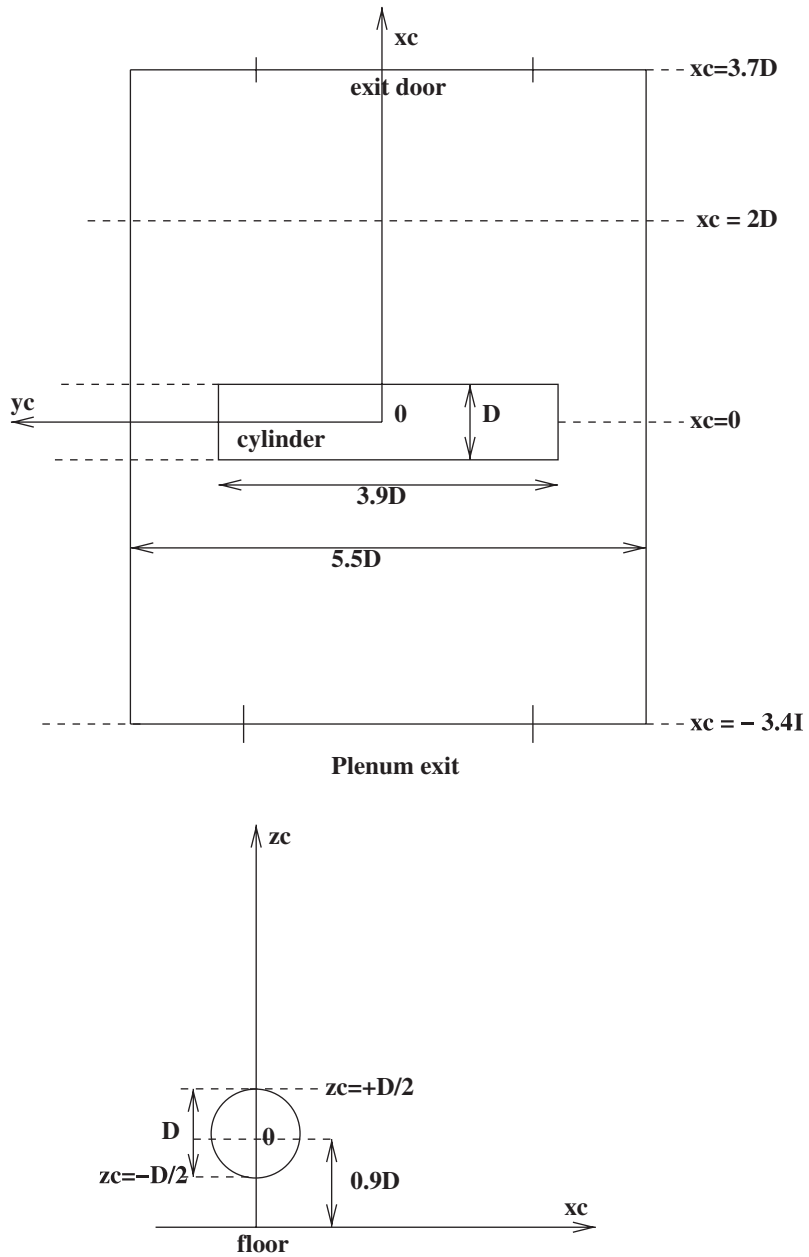

Figure 14. Layout of the facility using a different coordinate system, consistent with previous studies on flow over cylinders.

DOI: 10.1002/fld

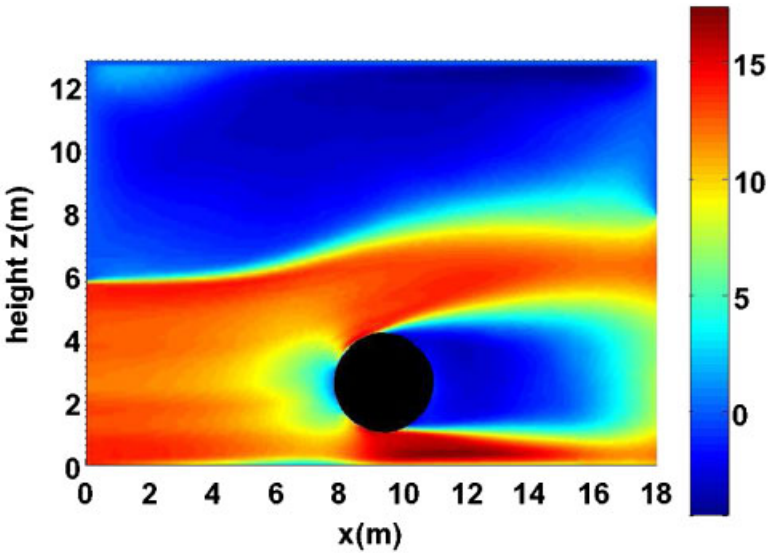

Figure 15. Time-averaged streamwise velocity at $y=0$.

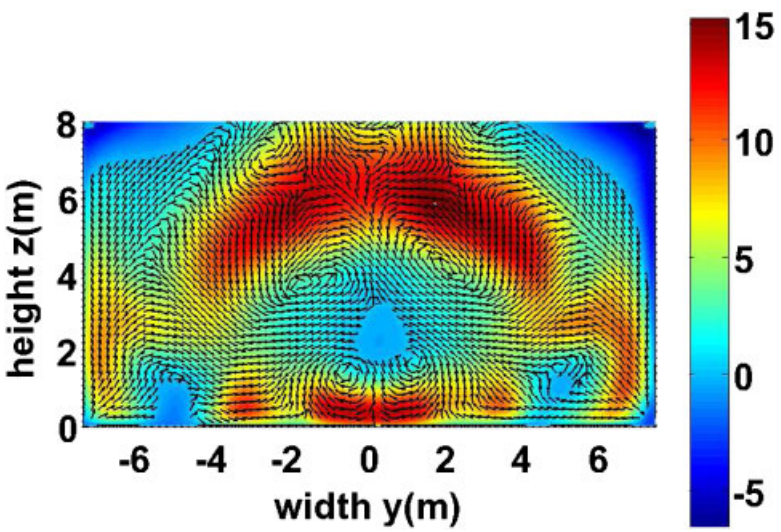

Figure 16. Time-averaged velocity vectors superimposed on the time-averaged streamwise velocity contours at $x=15$ m. Vectors are normalized by the norm of the 2-component-vector. For clarity, vectors are plotted every six points.

numerical results is excellent. For the case with the large cylinder, the size of the wake was very well reproduced. Similarly, the shedding frequency obtained from LES matched the value given in previous studies of a flow over free standing cylinders. The present LES model was also capable of predicting more detailed flow characteristics such as the stagnation and recirculation regions.

DOI: 10.1002/fld

It was found that the velocity magnitude was overpredicted in the wake region. This discrepancy with the experiments may come from a combination of factors involved in the present LES, such as the boundary layer resolution, the subgrid model and discretization errors. Overall, however, the LES results produced satisfactory predictions relative to the experimental uncertainty. They have proven to be an excellent engineering tool in cases where large vortex motion is expected to occur and will facilitate optimization of experimental design and instrumentation layouts for future tests in the facility.

ACKNOWLEDGEMENTS

Financial support by Natural Sciences and Engineering Research Council (NSERC) of Canada is gratefully acknowledged.

REFERENCES

1. Teunissen HW. Simulation of the planetary boundary layer in a multiple-jet wind tunnel. *Atmospheric Environment* 1975; **9**:145–174.
2. Nishi A, Miyagi HH. Computer-controlled wind tunnel for wind-engineering applications. *Journal of Wind Engineering and Industrial Aerodynamics* 1995; **54–55**:493–504.
3. Kikitsu H, Kanda J, Iwasaki R. Flow simulation by wind tunnel with computer-controlled multiple fans. *Journal of Wind Engineering and Industrial Aerodynamics* 1999; **88**:421–429.
4. Diana G, De Ponte S, Falco M, Zasso A. A new large wind tunnel for civil-environmental and aeronautical applications. *Journal of Wind Engineering and Industrial Aerodynamics* 1998; **74–76**:553–565.
5. Smith BE, Zell PT, Shinoda PM. Comparison of model- and full-scale wind tunnel performance. *Journal of Aircraft* 1990; **27**:232–238.
6. Lubcke H, Schmidt S, Rung T, Thiele F. Comparison of LES and RANS in bluff-body flows. *Journal of Wind Engineering and Industrial Aerodynamics* 2001; **89**:1471–1485.
7. Bosh G, Rodi W. Simulation of vortex shedding past a square cylinder with different turbulence models. *International Journal for Numerical Methods in Fluids* 1998; **28**:601–616.
8. Cheng Y, Lien FS, Yee E, Sinclair R. A comparison of large eddy simulations with a standard k–ε Reynolds-averaged Navier–Stokes model for the prediction of a fully developed turbulent flow over a matrix of cubes. *Journal of Wind Engineering and Industrial Aerodynamics* 2003; **91**:1301–1328.
9. Camarri S, Salvetti MV, Buresti G. Large-eddy simulation of the flow around a triangular prism with moderate aspect ratio. *Journal of Wind Engineering and Industrial Aerodynamics* 2006; **94**:309–322.
10. Franke J, Frank W. Large-eddy simulation of the flow past a circular cylinder at $Re_d = 3900$. *Journal of Wind Engineering and Industrial Aerodynamics* 2002; **90**:1191–1206.
11. Breuer M. A challenging test case for large eddy simulation: high Reynolds number circular cylinder flow. *International Journal of Heat and Fluid Flow* 2000; **21**:648–654.
12. Catalano P, Wang M, Iaccarino G, Moin P. Numerical simulation of the flow around a circular cylinder at high Reynolds numbers. *International Journal of Heat and Fluid Flow* 2003; **24**:463–469.
13. Mc Caffrey BJ, Hekestad G. A robust bidirectional low-velocity probe for flames and fire applications. *Combustion and Flame* 1976; **26**:125–127.
14. Doebelin EO. *Measurement Systems*: *Application and Design* (4th edn). McGraw-Hill: New York, 1990.
15. McGrattan K. *FDS Technical Reference Guide Version 4*. NIST, 2005.
16. McGrattan KB, Baum HR, Rehm RG. Numerical simulation of smoke plumes from large oil fires. *Atmospheric Environment* 1996; **30**:4125–4136.
17. Chung W, Devaud CB. Buoyancy-corrected k–ε models and large eddy simulation applied to a large axisymmetric helium plume. *International Journal for Numerical Methods in Fluids* 2008; DOI:10.1002/fld.1720.
18. Smagorinsky J. General circulation experiments with primitive equations—I. The basic experiments. *Monthly Weather Review* 1963; **91**:99–164.
19. Tanaka E, Nakata S. The interference of two-dimensional parallel jets. *Bulletin of the Japan Society of Mechanical Engineers* 1975; **18**:1134–1141.

20. Rajaratham N. *Turbulent Jets*. Elsevier: Amsterdam, 1976.
21. Baggett JS, Jimenez J, Kravchenko AG. Resolution requirements in large eddy simulations of shear flows. *Annual Research Briefs* 1997; 51–66.
22. Jiang Y, Alexander D, Jenkins H, Arthur R, Chen Q. Natural ventilation in buildings: measurement in a wind tunnel and numerical simulation with large-eddy simulation. *Journal of Wind Engineering and Industrial Aerodynamics* 2003; **91**:331–353.
23. Roshko A. Experiments on the flow past a circular cylinder at very high Reynolds number. *Journal of Fluid Mechanics* 1960; **10**:345–356.
24. Shih WCL, Wang C, Coles D, Roshko A. Experiments on flow past rough circular cylinders at large Reynolds numbers. *Journal of Wind Engineering and Industrial Aerodynamics* 1993; **49**:351–368.
25. Zdravkovich MM. *Flow Around Circular Cylinders*, *vol. 1*: *Fundamentals*. Oxford University Press: Oxford, 1997.
26. Huang JF, Zhou Y, Zhou T. Three-dimensional wake structure measurement using a modified PIV technique. *Experiments in Fluids* 2006; **40**:884–896.

DOI: 10.1002/fld